Available online at www.sciencedirect.com
ScienceDirect
Earth and Planetary Science Letters 264 (2007) 61–71
EPSL
www.elsevier.com/locate/epsl

Paleointensity of the Earth's magnetic field using SQUID microscopy

Benjamin P. Weiss [a,*], Eduardo A. Lima [a], Luis E. Fong [b], Franz J. Baudenbacher [b,c]

[a] Department of Earth, Atmospheric, and Planetary Sciences, Massachusetts Institute of Technology, Cambridge, MA 02139, USA
[b] Department of Physics and Astronomy, Vanderbilt University, Nashville, TN 37235, USA
[c] Department of Biomedical Engineering, Vanderbilt University, Nashville, TN 37235, USA

Received 17 May 2007; received in revised form 1 August 2007; accepted 28 August 2007
Available online 15 September 2007
Editor: C.P. Jaupart

Abstract

Knowledge of the paleointensity of magnetic fields is valuable for our understanding of the origin and evolution of planetary dynamos and the history of planetary interiors. Until recently, quantitative paleomagnetic and paleointensity analyses were limited to magnetometry of bulk samples. The most sensitive of these moment magnetometers use superconducting quantum interference devices (SQUIDs), which measure the net moment of samples typically millimeters to centimeters in size with sensitivities of 10^{-9} Am^2. Recently, SQUIDs have been adapted to map the fine-scale magnetic fields of geological thin sections with unprecedented spatial resolutions of better than 100 μm and moment sensitivities better than 10^{-15} Am^2. Here we present a detailed study of the magnetization within basalts from the Hawaii Scientific Drilling Project using SQUID microscopy and moment magnetometry in combination with borehole magnetometry, petrographic and geologic data. We demonstrate how SQUID microscopy can be used to measure the paleointensity of the Earth's field which magnetized these basalts during the last 500 ky. These experiments are the first time alternating field demagnetization and paleointensity experiments have been conducted on natural remanent magnetization using submillimeter magnetic imaging techniques. Our high resolution field maps enable us to make thousands of paleointensity measurements on a single thin section which can be correlated with the minerals, petrologic textures, and alteration zones within the samples.

Keywords: basalt; Hawaii Scientific Drilling Project; paleomagnetism; paleointensity; SQUID microscopy

1. Introduction

It is thought that Folgerhaiter was the first to suggest that the thermoremanent magnetization (TRM) in natural materials could be used to infer the intensity of the ancient magnetic field (Folgheraiter, 1899). Nearly four decades later, Koenigsberger (Koenigsberger, 1933) carried out important thermal analyses of natural remanent magnetization (NRM) and then Thellier (Thellier, 1937) demonstrated that a comparison of a sample's natural TRM with that produced by known laboratory field is an accurate paleointensity indicator. To avoid sample alteration often associated with the Thellier method, other (less accurate) paleointensity techniques have also been developed that involve normalizing the NRM to an artificial magnetization created without heating. It has been demonstrated from studies of a wide variety of

* Corresponding author.
E-mail address: bpweiss@MIT.EDU (B.P. Weiss).

0012-821X/$ - see front matter © 2007 Elsevier B.V. All rights reserved.
doi:10.1016/j.epsl.2007.08.038

terrestrial, and extraterrestrial minerals and their synthetic analogs that the ratio of a thermoremanent NRM to the saturation isothermal remanent magnetization (sIRM) is proportional to the intensity of the paleofield which produced the NRM (Kletetschka et al., 2004; Gattacceca and Rochette, 2004; Kletetschka et al., 2003; Fuller et al., 1988; Fuller and Cisowski, 1987; Fuller et al., 2002; Kletetschka et al., 2006; Verrier and Rochette, 2002). Samples containing approximately equant crystal shapes will have NRM/sIRM ~ several % for a single TRM component produced in Earth's field (~50 μT). For such samples, the paleointensity estimate from this technique typically has an uncertainty of about a factor of ~2–5, with the chief sources of error being the dependence of TRM intensity on the unknown grain volume and microscopic coercivity distribution (Yu, 2006).

All paleointensity techniques are limited by the fact that rocks contain complex mixtures of ferromagnetic crystals, only some of which are suitable for accurately recording paleofields. For instance, the paleointensity will be underestimated if the targeted NRM is not a pure TRM but rather a crystallization remanent magnetization (CRM) resulting from natural alteration of the sample. Such altered igneous rocks often have NRM/sIRM ~0.1% or lower because of the relative inefficiency of the CRM acquisition process (Fuller et al., 1988; Fuller et al., 2002). A persistent problem is that such alteration often is only present at spatial scales far smaller than the sample sizes typically measured with moment magnetometers. Secondly, only some phases in rocks have suitable crystal sizes and resistance to alteration during laboratory heating for paleointensity studies. To mitigate these kinds of problems, investigators have begun over the last decade to analyze carefully screened individual several millimeter diameter mineral and glass separates rather than whole rock samples (Pick and Tauxe, 1994; Cottrell and Tarduno, 1999). Nevertheless, these and all experiments to date have been conducted on bulk samples in the sense that a single paleointensity estimate is derived for each grain.

Here we describe a new paleointensity technique in which we derive tens of thousands of individual paleointensity measurements from a single cm-sized thin section that can be spatially correlated with mineralogical and petrographic textures. Our approach uses the low-transition temperature superconducting quantum interference device (SQUID) Microscope (SM) (Fong et al., 2005), a magnetometer that maps the vertical component of the magnetic field of room temperature samples with a spatial resolution of with 100–250 μm and moment sensitivity of better than 10^{-15} Am^2. SQUID microscopy has been used in previous paleomagnetic and rock magnetic studies (see Weiss et al., 2007 and references therein). For this study, we used the NRM/sIRM method as the first step for adapting SQUID microscopy to paleointensity experiments. The basic technique described here should in the future be adaptable to more robust methods like that of Thellier.

2. Samples

We studied two 25-cm diameter, 10-cm long cylindrical paleomagnetic cores (B0829-1 and B0829-2) and two 30-μm thin sections (B0829-3 and B0829-4) of subaqueously erupted tholeiitic basalt taken from the Hawaii Scientific Drilling Project (HSDP) 2 core through the Mauna Kea volcano, Hawaii. B0829-1 and-2 samples were originally from a depth of 2422.0m below sea level (mbsl) and B0829-3 and-4 from a depth of 2421.4mbsl (all four samples from core box 829, run 828). All have $^{40}Ar/^{39}Ar$ extrusive ages of ~500ka (Sharp and Renne, 2005). B0829-1,-2, and-3 were taken from the interior of two nearly unaltered aphyric vesicular pillows (DePaolo et al., 1999). B0829-4 is a transect across the outer part of a vesicular, nearly aphyric pillow and its sideromelane (basaltic glass) rind. Because the HSDP2 core is not azimuthally oriented, only the geographic inclination (not declination) of the NRM can be measured from these samples.

Our optical and electron microscopy data indicate that B0829-1, -2, and -3 as well as the interior of the pillow in B0829-4 consist of predominantly a groundmass of olivine, pyroxene, plagioclase, chromian spinel, titanomagnetite and interstitial glass and have abundant vesicles filled with nonmagnetic secondary minerals (predominantly chabazite and a spherulitic silica-rich pore-lining zeolite), similar to that previously observed for other HSDP samples (Baker et al., 1996; Walton and Schiffman, 2003; Schiffman et al., 2006). The titanomagnetite is pseudo single domain in size and has composition $0.6Fe_2TiO_4 \cdot 0.4Fe_3O_4$, a Curie temperature of 100–200 °C, a bulk coercivity of ~20 mT, and a squareness of ~0.4 (Kontny et al., 2003; Tauxe and Love, 2003). This combination of relatively low Curie point and elevated borehole temperatures means that its NRM is a viscous remanence acquired in the recent geomagnetic field; Thellier–Thellier paleointensity experiments on the core (Tauxe and Love, 2003) indicate that this field has an average intensity of 50–60 μT. The outer 2-mm edge of the B0829-4 pillow is mineralogically and compositionally zoned, transitioning from an innermost zone of microcrystalline groundmass (innermost zone), to sideromelane, to palagonite (altered sideromelane) and ultimately to the spherulitic zeolite rind.

3. Magnetic methods

Moment magnetometry measurements of bulk samples B0829-1, B0829-2, and thin section B0829-3 were taken with 2G Enterprises Superconducting Rock Magnetometers (2G) inside a single mu-metal layer magnetically shielded room (DC field <150 nT) in the MIT Paleomagnetism Laboratory and a transform-steel magnetically shielded room in the Caltech Paleomagnetics Laboratory (DC field <1000 nT) (Fig. 1A,B,C) . The 2G uniquely measures the net moment and direction of individual samples. We measured the evolution of the sample NRMs during a series of progressive three-axis alternating field (AF) demagnetization treatments up to a peak field of 2800 mT. Previous magnetic studies of HSDP cores have demonstrated that magnetic

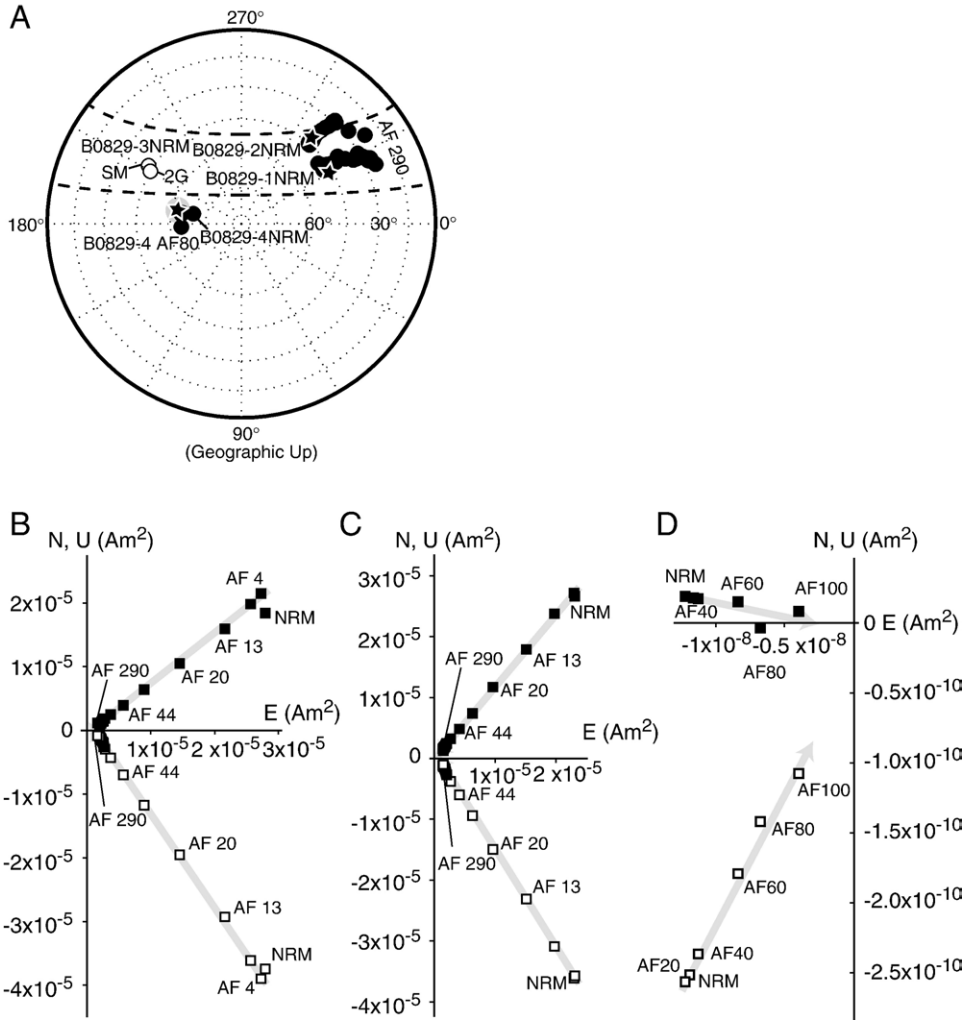

Fig. 1. Natural remanent magnetization (NRM) and progressive alternating field (AF) demagnetization of the basalt samples from the Hawaii Scientific Drilling Project 2. (A) Equal area plot showing directions of core samples B0829-1 and B0829-2 (measured with a 2G Enterprises Superconducting Rock Magnetometer (2G)), thin section B0829-3 (measured with 2G and as inferred from inversions of SQUID microscopy (SM) data), and thin section B0829-4 (inferred from inversions of SM data). Open (closed) symbols represent upper (lower hemisphere). Also shown is the range of magnetic inclination measured in the HSDP2 borehole using a fluxgate magnetometer over the depth range 2421–2422 mbsl (Steveling, personal communication); transformed into core coordinates, these inclination data map as a minor circle band on the equal area plot (boundaries delineated by two dashed lines). Stars denote characteristic magnetization directions obtained from principle component analyses. Surrounding grey ovals have a diameter equal to the maximum angular deviation associated with these fits. (B, C, D) Evolution of magnetization vector during progressive AF demagnetization of B0829-1 (B), B0829-2 (C), and B0829-4 (D). Closed (open) symbols represent end points of magnetization projected onto horizontal (vertical) planes. Peak fields for each AF step are labeled in mT. Grey arrows indicate characteristic magnetization directions obtained from principle component analysis. All directions are in core coordinates, for which the HSDP borehole axis up/geographic up has inclination $i = 0°$ declination $\delta = 90°$ in (A) and is South and horizontal in (B–D).

inclinations derived from AF and thermal demagnetization are similar (Laj and Kissel, 1999; Holt and Kirschvink, 1996). Following AF demagnetization, we conducted a variety of 2G rock magnetic experiments including anhysteretic remanent magnetization (ARM) acquisition, isothermal remanent magnetization (IRM) acquisition and alternating field demagnetization of ARM and IRM, and back-field IRM acquisition to measure grain-size, degree of magnetostatic interactions, sIRM (Cisowski, 1981) and coercivity of remanence. These experiments (data not shown) are consistent with the samples containing PSD titanomagnetite.

The NRM field and the sIRM fields of thin sections B0829-3 and B0829-4 were measured with the SM inside a three-layer mu-metal shielded room (DC field <50 nT and AC field peak-to-peak variations <0.05 nT at 0.01 Hz) (Figs. 1A,B,C, 2, 3). Each SM scan consists of a grid of thousands of individual measurements of the vertical component of the magnetic field taken at a constant height above a room-temperature sample. Unlike the 2G, the SM maps field rather than magnetization; magnetization must be constrained from inversions of the field data. The NRM and sIRM fields of B0829-3 (Fig. 2) were taken entirely using a 120-μm diameter monolithic DC SQUID sensor (Baudenbacher et al., 2003) and were also measured with the 2G (Fig. 1A).

B0829-4 was scanned multiple times with the SM in the course of progressive AF demagnetization, with peak fields increasing from 20 to 100 mT in steps of 20 mT (Figs. 1D, 3). SM scans of B0829-4 were taken using two different sensors: a 250-μm diameter superconducting pickup coil inductively coupled to a Quantum Design DC SQUID (Fig. 3C, E–I) and also directly with a 120-μm diameter monolithic SQUID sensor (Baudenbacher et al., 2003) (Fig. 3D). Further details of sample preparation, instrument operation, noise level, and data processing can be found in (Weiss et al., 2007).

4. Measurements

The 2G measurements of the two bulk samples B0829-1 and-2 revealed similar NRM demagnetization behaviors. Each had a single predominant magnetization component accounting for at least 96% of the total NRM and carried by grains with effective coercivities from near 0 to >280 mT (Fig. 1A-C, Tables 1, 3). Because the sample moments did not decay directly to the origin during AF demagnetization, they must also have a weak (intensity ≤4% of NRM) higher coercivity component. Predominantly one-component demagnetization behavior is characteristic of much of the HSDP core (Tauxe and Love, 2003; Laj and Kissel, 1999; Holt and Kirschvink, 1996). The characteristic directions obtained from principle component analysis (PCA) line fits (Kirschvink, 1980) in geographic coordinates have inclination of $i' = 24 \pm 0.8°$ and $i' = 27 \pm 0.6°$ for B0829-1 and B0829-2, respectively (Fig. 1A–C, Table 2) (uncertainties are maximum angular deviation (MAD)). Given that records of magnetic inclination often show rapid spatial variability due to past secular variation, these values agree well with the range of HSDP2 borehole logging inclinations measured at these depths of $i' = 12$ to 38° (Steveling et al., 2003; Steveling, 2006) (Fig. 1). NRM/sIRM for B0829-1 and-2 are 4.6% and 3.9%, respectively, consistent with a TRM (or viscous remanence) acquired in a field of several tens of microteslas (equal to that at the surface of the present-day Earth) (Table 1).

The technical aspects of our measurements and inversion analysis of thin section B0829-3 are described in detail elsewhere (Weiss et al., 2007). To summarize, the 2G measured an NRM of $m = 6.4 \times 10^{-8}$ Am^2,

Table 1
Summary of paleointensity estimates

Sample	Type	Instrument	m (Am^2)*	i (°)*	i' (°)*	δ (°)*	NRM/sIRM§
B0829-1	NRM	2G	5.0×10^{-5}	48	21	320	4.6%
	sIRM	2G	1.1×10^{-3}†	−83	3	335	(bulk)
B0829-2	NRM	2G	5.1×10^{-5}	45	33	310	3.9%
	sIRM	2G	1.3×10^{-3}†	−86	2	327	(bulk)
B0829-3	NRM	2G	6.4×10^{-8}	−45	21	210	2.9%
	sIRM	2G	2.2×10^{-6}	−90	0	2	(bulk)
	NRM	SM	9.0×10^{-8}	−43	23	212	5.6%
	sIRM	SM	1.6×10^{-6}	−90	0	0	(bulk)
B0829-4	NRM	SM	2.7×10^{-9}	−65	4	189	3.6%
	sIRM	SM	3.1×10^{-8}	−90	0	0	(bulk)
							0.82% (pal)
							3.9% (inter)

i=magnetic inclination in core coordinates, i'=magnetic inclination in geographic coordinates, δ=magnetic declination in core coordinates, NRM/sIRM=the ratio of the natural remanent magnetization (NRM) to the saturation isothermal remanent magnetization (sIRM) for each sample, AF n=alternating field demagnetization to peak field of n mT, 2G=2G Enterprises Superconducting Rock Magnetometer, SM=SQUID Microscope. See Fig. 1 for definition of core coordinates.

*For NRM, AF, and sIRM steps, these values are from direct measurements for the 2G and from inversions of field data for SM.

†Because the sIRM values for B0829-1 and B0829-2 exceed the maximum that is measurable with the 2G, these values are inferred from the average of sIRM measurements of two subsamples from each core, scaled by the mass ratio of the parent core to each subsample.

§bulk=total NRM divided by total sIRM; pal=median NRM/sIRM for all pixels in palagonite rind; inter=median NRM/sIRM for all pixels in pillow interior (see Fig. 5E).

inclination $i = -45 \pm 3°$ in core coordinates ($i' = 22.0 \pm 3°$ in geographic coordinates) and clockwise core coordinate declination of $\delta = 210 \pm 3°$, again in excellent agreement with the borehole data (Steveling et al., 2003; Steveling, 2006) (Fig. 1A). Angular uncertainties for all 2G measurements are one circular standard deviation as inferred from four or eight repeated measurements. Using the 2G measurement of sIRM (2.2×10^{-6} Am^2), this again gives an NRM/sIRM of several percent, indicating a TRM formed in a field of several tens of microteslas (Table 1).

SM measurements of both the NRM and sIRM of B0829-3 revealed a spatially heterogeneous field with high intensity and positive (out-of-the-plane of the thin section) orientation above titanomagnetite-rich regions and weak and negative (into-the-plane) orientation above vesicles and outside the boundaries of the thin section (Fig. 2). Least squares magnetization fits to the NRM and sIRM data indicate that the magnetization within the pillow is predominantly unidirectional but has spatially nonuniform intensity positively correlated with the titanomagnetite-rich groundmass. The total NRM and sIRM for these solutions (sum of all data in Fig. 2E and F, respectively) are within error of direct 2G measurements of the very same thin section (Fig. 1A and Tables 1, 3). NRM/sIRM obtained from both the 2G data and from the summed SM inversion solutions are again several percent (Table 1).

But the SM images actually afford the possibility of going far beyond 2G bulk paleointensity measurements by directly imaging NRM/sIRM across the thin section. Dividing the NRM and sIRM solutions yields a map of more than *fifteen thousand* individual paleointensity measurements (Fig. 2G,H and Table 1). Each such measurement is drawn from $\sim 3 \times 10^{-13}$ m^3 ($\sim$90 ng) of

Table 2
Characteristic magnetization directions

Sample	Steps	Instrument	i (°)	i' (°)	δ (°)	MAD (°)
B0829-1	AF 4–AF 290	2G	49	24	322	0.8
B0829-2	NRM–AF 290	2G	46	27	310	0.6
B0829-3	NRM	2G	−45	21	210	–
	NRM	SM	−43	23	212	–
B0829-4	NRM–AF 100	SM	62	6	192	5.2

Note: shown are the characteristic natural remanent magnetization directions inferred from principle component analyses (PCA) of the listed measurement steps following [28]. i=magnetic inclination in core coordinates, i'=magnetic inclination in geographic coordinates, δ=magnetic declination in core coordinates, MAD=maximum angular deviation from PCA, NRM=natural remanent magnetization, AF n=alternating field demagnetization to peak field of n mT, 2G=2G Enterprises Superconducting Rock Magnetometer, SM=SQUID Microscope. See Fig. 1 for definition of core coordinates.

Table 3
Natural remanent magnetization and demagnetization measurements

Sample	Type	Instrument	m (Am^2)*	i (°)*	δ (°)*	CSD (°)
B0829-1	NRM	2G	5.0×10^{-5}	48	320	0.5
	AF 4	2G	5.2×10^{-5}	48	322	0.6
	AF 9	2G	4.9×10^{-5}	48	322	0.9
	AF 13	2G	4.0×10^{-5}	48	324	0.9
	AF 19	2G	2.7×10^{-5}	48	324	0.6
	AF 29	2G	1.6×10^{-5}	47	324	0.5
	AF 44	2G	9.8×10^{-6}	45	325	0.5
	AF 66	2G	6.2×10^{-6}	44	326	0.7
	AF 85	2G	4.5×10^{-6}	41	327	0.6
	AFz 100	2G	4.1×10^{-6}	39	325	0.5
	AFz 120	2G	$3.8 \times 10^{--6}$	37	328	0.7
	AFz 140	2G	3.5×10^{-6}	34	330	0.4
	AFz 160	2G	3.3×10^{-6}	32	331	0.9
	AFz 180	2G	3.1×10^{-6}	31	329	1.1
	AFz 200	2G	2.9×10^{-6}	29	331	0.7
	AFz 220	2G	2.8×10^{-6}	28	333	0.4
	AFz 240	2G	2.6×10^{-6}	26	333	1.3
	AFz 260	2G	2.5×10^{-6}	26	335	0.8
	AFz 280	2G	2.4×10^{-6}	25	336	0.8
	AFz 290	2G	2.2×10^{-6}	23	324	0.5
B0829-2	NRM	2G	5.1×10^{-5}	45	310	0.8
	AF 4	2G	5.0×10^{-5}	45	311	0.7
	AF 9	2G	4.4×10^{-5}	45	310	1.2
	AF 13	2G	3.3×10^{-5}	45	310	1.2
	AF 19	2G	2.1×10^{-5}	45	310	0.8
	AF 29	2G	1.4×10^{-5}	44	310	1.1
	AF 44	2G	8.7×10^{-6}	43	311	1.3
	AF 66	2G	5.7×10^{-6}	42	310	1.1
	AF 85	2G	4.2×10^{-6}	40	310	0.9
	AFz 100	2G	3.9×10^{-6}	39	310	1.5
	AFz 120	2G	3.7×10^{-6}	37	311	0.9
	AFz 140	2G	3.4×10^{-6}	35	311	0.6
	AFz 160	2G	3.2×10^{-6}	33	312	1.0
	AFz 180	2G	3.0×10^{-6}	32	312	0.7
	AFz 200	2G	2.9×10^{-6}	31	312	0.9
	AFz 220	2G	2.7×10^{-6}	30	312	1.7
	AFz 240	2G	2.6×10^{-6}	30	313	1.5
	AFz 260	2G	2.5×10^{-6}	30	313	1.7
	AFz 280	2G	2.4×10^{-6}	29	312	1.6
	AFz 290	2G	2.2×10^{-6}	28	319	1.6
B0829-3	NRM	2G	6.4×10^{-8}	−45	210	3.0
	NRM	SM	9.0×10^{-8}	−43	212	–
B0829-4	NRM	SM	2.7×10^{-9}	−65	189	–
	AF 20	SM	2.8×10^{-9}	−65	189	–
	AF 40	SM	2.6×10^{-9}	−65	189	–
	AF 60	SM	2.0×10^{-9}	−65	190	–
	AF 80	SM	1.6×10^{-9}	−65	177	–
	AF 100	SM	1.2×10^{-9}	−69	192	–

i=magnetic inclination in core coordinates, δ=magnetic declination in core coordinates, NRM=total natural remanent magnetization, CSD=circular standard deviation of magnetization direction as inferred from 4 or 8 repeat measurements, AF n=three-axis alternating field demagnetization to peak field of n mT, AFz n=vertical-axis alternating field demagnetization to peak field of n mT, 2G=2G Enterprises Superconducting Rock Magnetometer, SM=SQUID Microscope. For definition of core coordinates, see Fig. 1.
*For the 2G, these values are from direct measurements and for the SM, they are from inversions of field data.

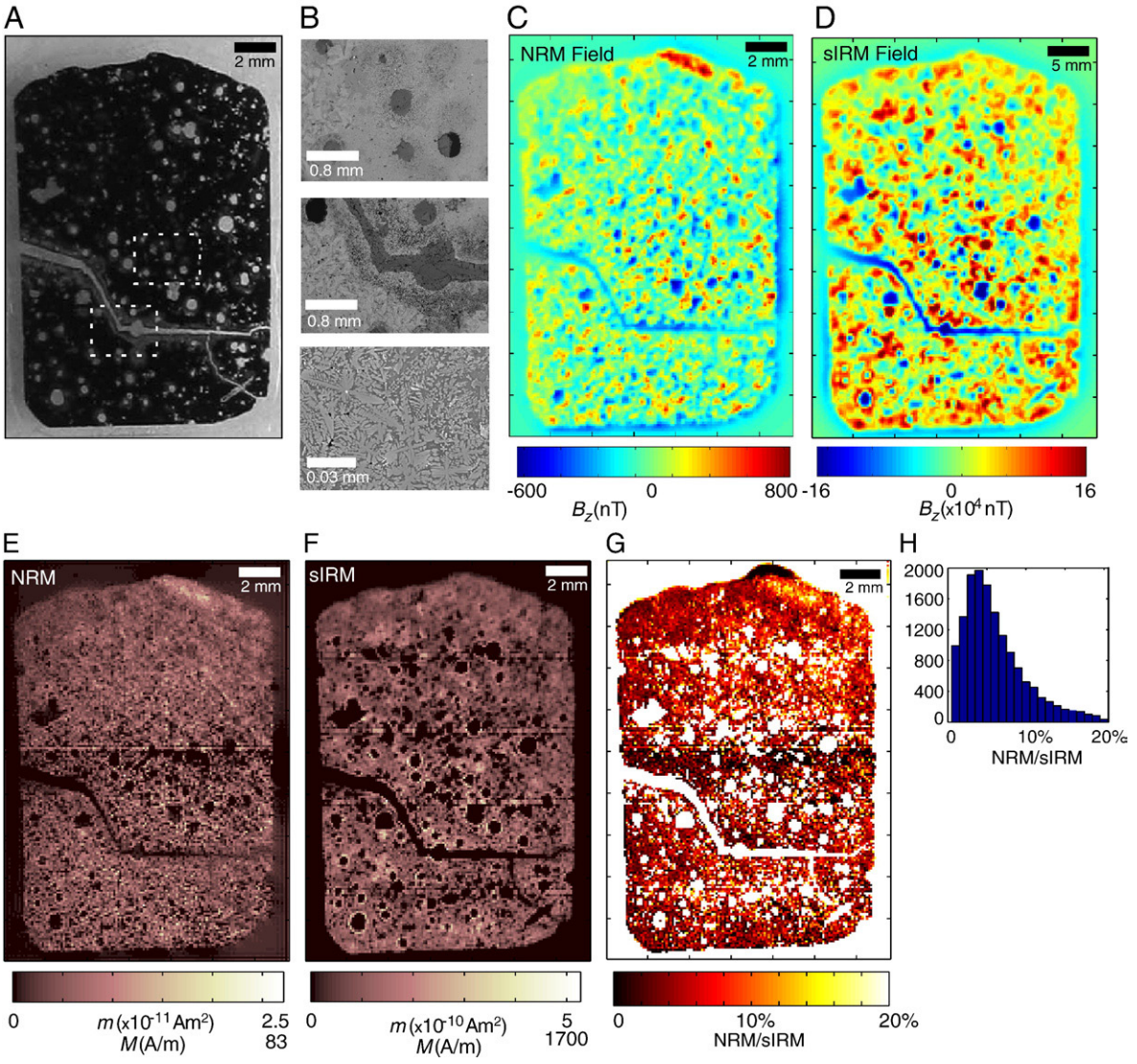

Fig. 2. SQUID Microscope (SM) paleointensity study of thin section B0829-3. (A) Reflected light photograph of thin section, showing groundmass of olivine, clinopyroxene, plagioclase, and titanomagnetite (dark areas) and numerous clear vesicles containing relatively nonmagnetic secondary minerals, primarily zeolites. Dashed boxes show locations of images in top and middle frames of (B). (B) Backscattered scanning electron microscopy images of basalt in (A). Top: typical vesicles filled with chabazite and surrounded by groundmass and olivine phenocrysts. Middle: crack running through lower middle of basalt filled with chabazite and surrounded by halo of groundmass in which the glass has apparently been dissolved (mottled areas) Bottom: quenched groundmass crystals surrounded by interstitial glass. (C) SM scan showing the vertical component of the natural remanent magnetization (NRM) field as measured at 25,976 locations ~190 μm above the sample. Same field of view as (A). (D) SM scan showing the saturation isothermal remanent magnetization (sIRM) field of the basalt thin section as measured at 25,976 locations ~190 μm above the sample (same field of view as (A)). The orientation of the saturating field was out of the page. (E) Best fit magnetic moments and magnetization of each of 25,976 dipoles from a unidirectional magnetization least squares fit to the NRM field (B). (F) Best fit magnetic moments of each of 25,976 dipoles from a unidirectional magnetization least squares fit to the sIRM field (D). (G) NRM/sIRM as calculated from the unidirectional magnetization fits (E, F). In nonmagnetic regions (vesicles, cracks and the quartz slide outside the boundaries of the thin section) where NRM/sIRM is undefined it was arbitrarily set to infinity. (H) Histogram of NRM/sIRM estimates for data points in (G).

basalt and, based on the moment intensities in Fig. 2F, millions of titanomagnetite crystallites. The results show that the groundmass has an average NRM/sIRM of 6% and a modal value of 4% with generally no major variability across the sample (NRM/sIRM of the vesicles and outside the thin section is undefined due to the lack of magnetic carriers in these areas). The spread of NRM/sIRM values (with a high-field tail out to ~20%) (Fig. 2H) likely is a reflection of the varying grain size of titanomagnetite throughout the sample (see

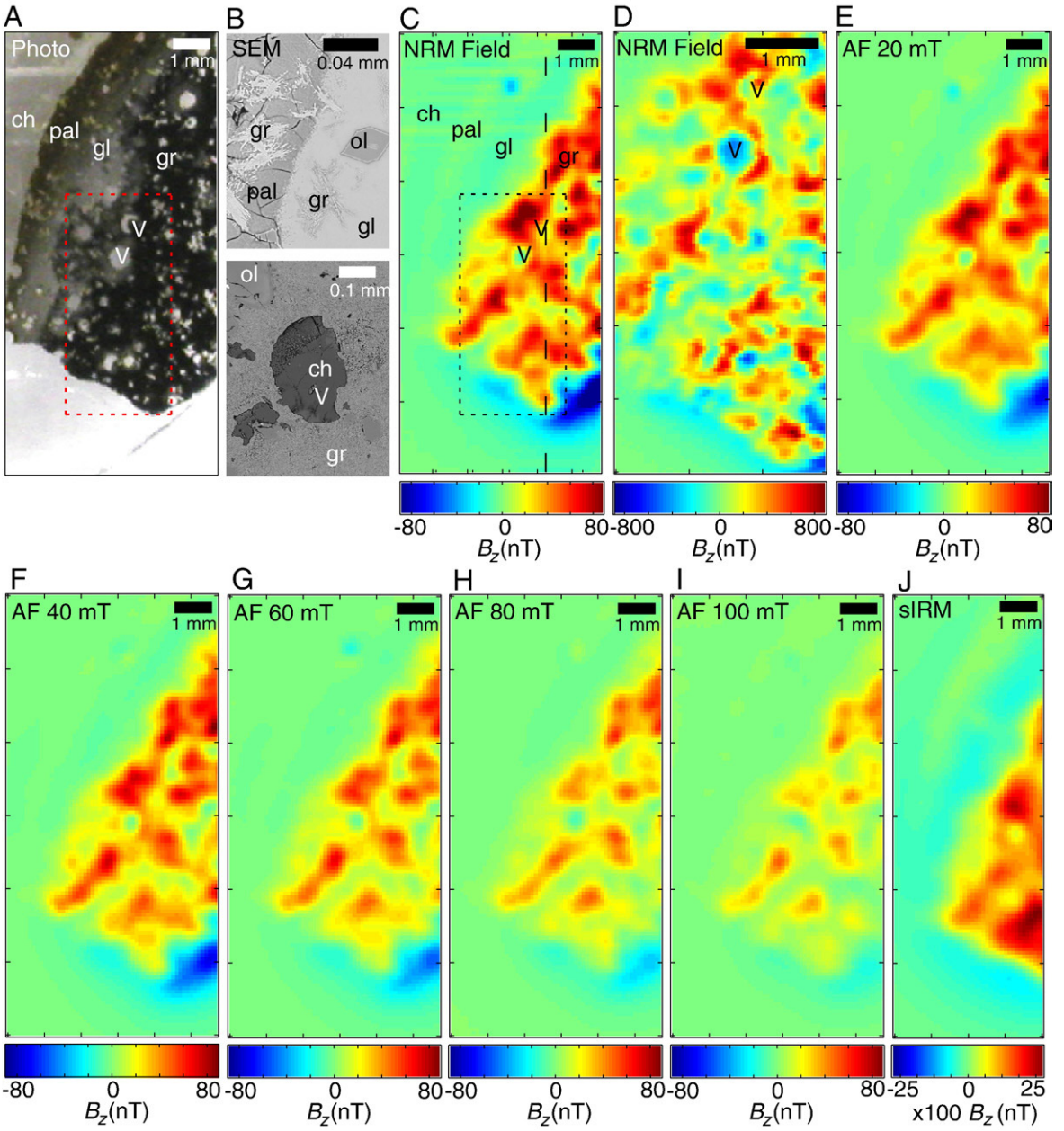

Fig. 3. SQUID Microscope (SM) measurements of thin section B0829-4. (A) Reflected light photograph of thin section, showing groundmass (gr) of olivine, clinopyroxene, plagioclase, and titanomagnetite (dark areas), numerous clear vesicles (V), light grey glassy rind (gl), orange palagonite outer rind (pal), and exterior chabazite (Cb). (B) Backscattered scanning electron microscopy images of basalt pillow in (A). Top: transition edge of pillow between palagonite zone at left and glass zone at right. Pillow interior is to the right. Small variolites of groundmass crystals are visible in both zones, and an olivine phenocryst is within the glass. The spatial density of variolites increases inward toward the right, eventually becoming continuous groundmass. Bottom: typical vesicle filled with chabazite and surrounded by groundmass and several olivine phenocrysts. (C) Scan showing the vertical component of the natural remanent magnetization (NRM) field ~230 μm above the sample measured using the SM equipped with a 250 μm diameter superconducting pickup coil sensor. Measurement was taken at a height of ~310 μm and data were then downward-continued (Blakely, 1996) to a height of 230 μm to match subsequent scans. Same field of view as (A). (D) Scan of dashed box region in (C) showing the vertical component of the NRM field ~120 μm above the sample measured using SM equipped with a 120 μm diameter monolithic SQUID sensor. Same vesicles shown in (A) are labeled. (E–I) SM scan of same field of view as (A) after three-axis alternating field (AF) demagnetization to 20 mT (E), 40 mT (F), 60 mT (G), 80 mT (H), and 100 mT (I). Shown is the magnetic field following AF demagnetization to each peak field at a height of 230 μm above sample. (J) SM scan of saturation isothermal remanent magnetization (sIRM) field ~230 μm above area to left of vertical dashed line in (C). Due to accidental sample misalignment, only part of the same field of view as the NRM was scanned. Scale bars are top right of each image.

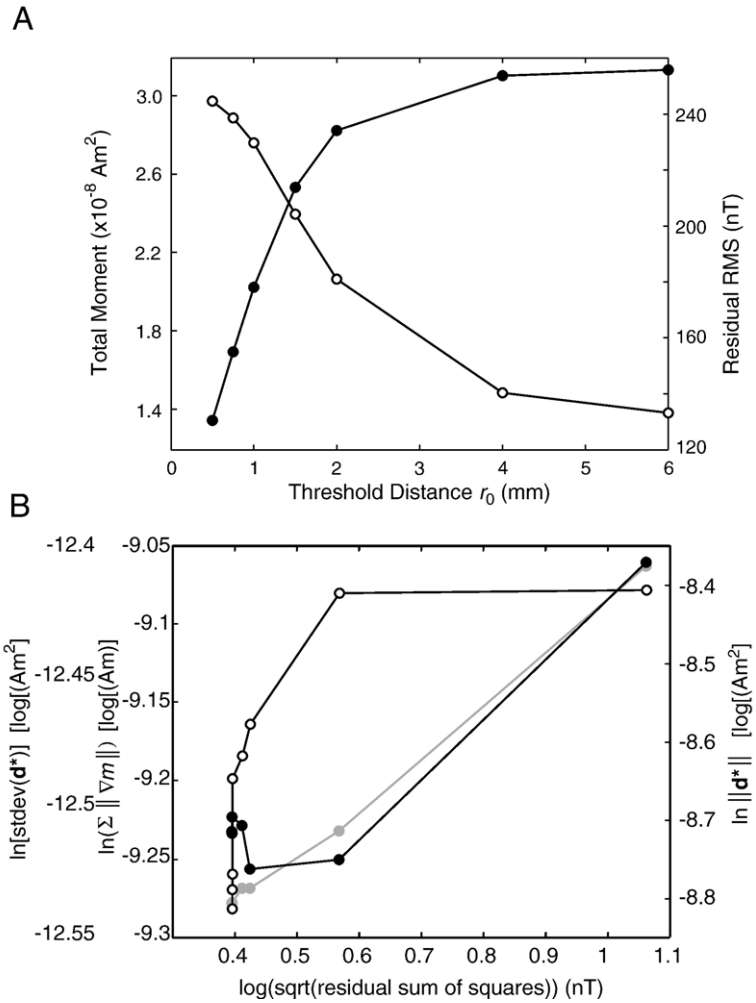

Fig. 4. Examples of numerical experiments used to determine optimal least squares parameters for fitting the unidirectional solution for B0829-4. See (Weiss et al., 2007) for details. (A) Effect of truncation of long range dipole interactions on the saturation isothermal remanent magnetization (sIRM) solution. Shown is the residual root mean square (RMS) difference between the data and the forward model (open circles) and total dipole moment of the solution (closed circles), each plotted as a function of threshold distance r_0. The total moment for r_0=6 mm shown here is given by the sum of the values in Fig. 5D. The residual RMS for r_0=6 mm shown here is given by the square root of the ratio of the residuals associated with this fit. (B) Effect of the maximum number iterations on the stability of the AF 60 mT solution using a Jacobian with r_0=6 mm. Shown is the Euclidean norm ‖**d***‖ (gray circles), standard deviation stdev(**d***) (solid black circles), and the summed gradient ∑‖∇*m*‖ (open black circles) for various solutions d* as a function of residual RMS. The shapes and slopes of these curves (concave down with the norm, derivative and standard deviation all generally decreasing with residual RMS) indicate that the inversion is not unstable like that exemplified by the L-shaped curves typical of ill-posed problems (see Weiss et al., 2007).

Yu, 2006). This ability to map paleointensities highlights the power of SQUID microscopy to generate large numbers of individual measurements in an automated manner that can be spatially correlated with the petrographic textures and mineralogy of a sample.

Our SM scans of the NRM of the pillow interior B0829-4 also revealed a unidirectional NRM with high intensity in the groundmass and negligible intensity in the vesicles and chabazite cement surrounding the pillow (Fig. 3). Least squares fits for magnetization using a truncation threshold r_0=6 mm (Fig. 4A) and an optimal number of iterations (Fig. 4B) (empirically determined following the methods of (Weiss et al., 2007) show that the sideromelane and palagonite rinds are weakly magnetized (Fig. 5), with the former being virtually undetectable due to the large demagnetizing field of the adjacent pillow interior. SM images taken during progressive AF demagnetization revealed that like our other HSDP samples, B0829-4 has a single component of magnetization extending to coercivities >100 mT (Fig. 1A,D). Given that we estimate the geographic orientations of our thin sections have an accuracy of ~5–10°, the geographic inclinations of the

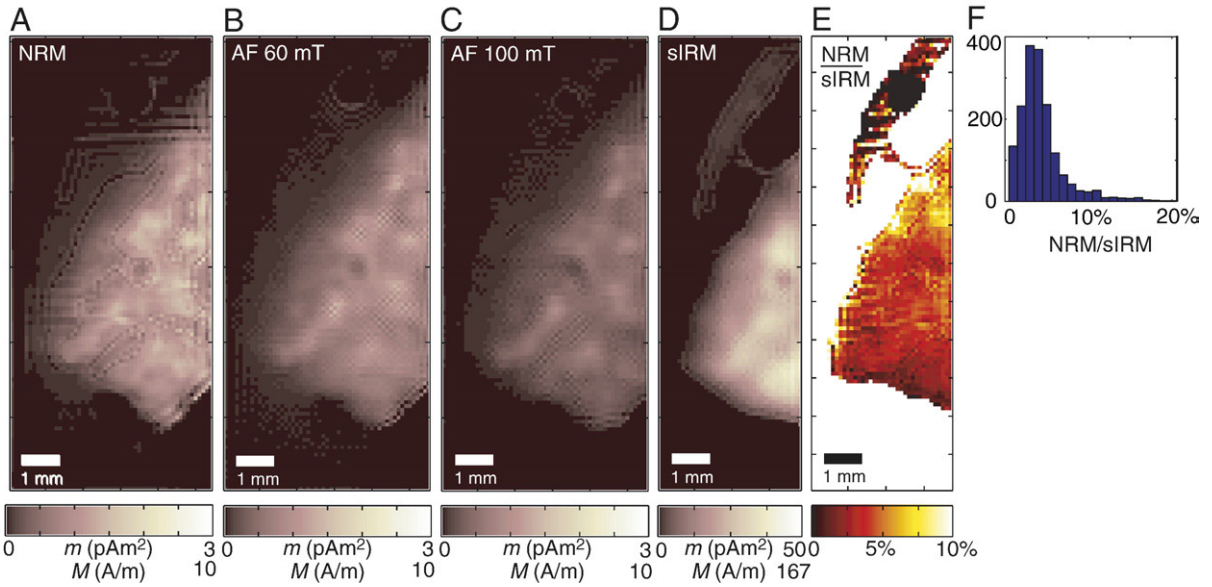

Fig. 5. Magnetization models inferred from SQUID Microscope scans of thin section B0829-4. (A) Best fit magnetic moments (magnetization when volume normalized) of each of 7018 dipoles from a unidirectional magnetization least squares fit to the NRM field (Fig. 3C). (B) Best fit magnetic moments of each of 7018 dipoles from a unidirectional magnetization least squares fit to the AF 60 mT demagnetization step (Fig. 3G). (C) Best fit magnetic moments (magnetization when volume normalized) of each of 7018 dipoles from a unidirectional magnetization least squares fit to the AF 100 mT field (Fig. 3I). (D) Best fit magnetic moments (magnetization when volume normalized) of each of 7018 dipoles from a unidirectional magnetization least squares fit to the sIRM field (Fig. 3J). The magnetization direction was required to have 90° inclination to match the direction of the applied field.(E)NRM/sIRM as calculated from the unidirectional magnetization fits (A, D). In nonmagnetic regions (vesicles, cracks and the quartz slide outside the boundaries of the thin section) where NRM/sIRM is undefined it was arbitrarily set to infinity. (F) Histogram of NRM/sIRM estimates for data points in (E).

individual demagnetization steps as well as that of the characteristic magnetization direction inferred from PCA line fits to all steps are generally in agreement with the borehole data from the same depth range (Fig. 1A,D and Tables 1, 2 and 3).

The NRM/sIRM distribution inferred from our inversion solutions (Fig. 5E,F and Table 1) has average and modal values of 4% and 3%, respectively. As before, this would indicate a TRM in the Earth's field. However, maps of NRM/sIRM indicate that only the pillow interior, which dominates the bulk magnetization because it contains nearly all of the magnetization in the thin section, has such a high value. NRM/sIRM within the palagonite rind is roughly five times weaker. If we assume the rind and interior both carry a TRM, then this discrepancy cannot be a reflection of differences in cooling rate on TRM efficiency because (a) the palagonite rind has a *more* intense NRM relative to the fresh glass rind which is *interior* to it and (b) theoretical considerations and experimental data indicate that it would be highly unlikely that the slight differences in cooling rate between two samples only several mm apart could produce an order of magnitude difference in paleointensity (Carlut and Kent, 2002). A second possible explanation of the lower NRM/sIRM in the palagonite rind relative to the pillow interior is that it is solely a result of a difference in crystal sizes (finer in the rim than the interior), again assuming both have the same ferromagnetic phases and carry a TRM. However, if anything, the data of (Yu, 2006) would predict that under this scenario the pillow interior, which contains pseudo single domain crystals, should have *lower* NRM/sIRM than the single domain crystals that dominate the remanence of glassy rinds.

Of course, it is almost certainly incorrect to assume that the palagonite and pillow interior have the same ferromagnetic mineralogy. The fact that the glass rind has a much lower sIRM than the palagonite exterior to it implies that the palagonite, which is a known alteration product, contains secondary ferromagnetic minerals such that the net saturation magnetization of the palagonite is greater than the glass. Additional secondary ferromagnetic minerals in the palagonite are required because numerous studies have documented that within the outer several mm of *unaltered* pillows, saturation remanence in sideromelane increases inward from the pillow margin as the result of an increasing concentration of crystalline phases (Carlut and Kent, 2002; Kent and Gee, 1996)

(a trend opposite to that observed here). Indeed, palagonite forms at low-temperature (<100 °C) and is known to contain secondary ferromagnetic minerals like hematite and goethite in addition to lithogenic magnetite (Stroncik and Schminke, 2002; Morris et al., 2001; Furnes, 1980). Therefore, the low paleointensity values in the palagonite can be readily explained as the product of an inefficiently magnetized alteration CRM (see Fuller et al., 1988; Fuller et al., 2002.

5. Summary

Our paleointensity experiments on samples from the interiors of fresh basalt pillows from Mauna Kea, Hawaii gave values of a few tens of microteslas. This is as expected for samples carrying a viscous remanence acquired in the Earth's day field over the last 500 ky and matches the results of previous paleointensity investigations (Kontny et al 2003; Tauxe and Love, 2003). Our experiments include the first alternating field demagnetization and first paleointensity experiments using submillimeter magnetic imaging techniques (although we note that electron holography has recently been used to study AF demagnetization (Feinberg, personal communication, 2007)). We have also demonstrated for the first time how SQUID Microscope data are in agreement with that of the 2G as well as the HSDP borehole fluxgate. SQUID microscopy generates thousands of individual paleomagnetic, rock magnetic, and paleointensity experiments on a single thin section. This has enabled us to obtain accurate paleointensity data from the interior of pillow whose palagonite rind gives paleointensities an order of magnitude too low. This illustrates how the imaging capability of SQUID microscopy can be used to obtain accurate paleointensity estimates from altered and heterogeneous samples which would be inaccessible to standard moment magnetometers. Future SQUID microscopy experiments incorporating the robust Thellier–Thellier paleointensity technique should further extend the power of this technique.

Acknowledgement

We thank R. Bennett-Calorio, M. Pendleton, J. Wikswo, C. Dwyer, and K. McBride for assistance with the measurements, J. Kirschvink for use of the CalTech 2G, I. Ceraj for computing tips, E. Steveling for sharing his unpublished HSDP2 borehole magnetic data, L. Carporzen and two anonymous reviewers for critical comments on the manuscripts, and N. Gitahi and C. Seaman for assistance with sampling the HSDP core. B. Weiss and F. Baudenbacher thank the NSF Geophysics and Instrumentation and Facilities Programs and the NASA Mars Fundamental Research and Planetary Major Equipment Programs. This paper is dedicated to the memory of Bill Goree.

References

Baker, M.B., Alves, S., Stolper, E.M., 1996. Petrology and petrography of the Hawaii Scientific Drilling Project lavas: inferences from olivine phenocryst abundances and compositions. J. Geophys. Res. 101, 11715–11727.

Baudenbacher, F., Fong, L.E., Holzer, J.R., Radparvar, M., 2003. Monolithic low-transition-temperature superconducting magnetometers for high resolution imaging magnetic fields of room temperature samples. Appl. Phys. Lett. 82, 3487–3489.

Blakely, R.J., 1996. Potential Theory in Gravity and Magnetic Applications. Cambridge University Press, New York. (441 pp).

Carlut, J., Kent, D.V., 2002. Grain-size-dependent paleointensity results from very recent mid-oceanic ridge basalts. J. Geophys. Res. 107. doi:10.1029/2001JB000439.

Cisowski, S., 1981. Interacting vs. non-interacting single-domain behavior in natural and synthetic samples. Phys. Earth Planet. Inter. 26, 56–62.

Cottrell, R.D., Tarduno, J.A., 1999. Geomagnetic paleointensity derived from single plagioclase crystals. Earth Planet. Sci. Lett. 169, 1–5.

DePaolo, D.J., Stolper, E.M., Thomas, D.M., Garcia, M.O., 1999. Hawaii Scientific Drilling Project: Core logs and summarizing data. Pasadena.

Folgheraiter, M., 1899. Sur les variations seculaires de l'inclinaison magnetique dans l'antiquite. J. de Physique 8, 660–667.

Fong, L.E., Holzer, J.R., McBride, K.K., Lima, E.A., Baudenbacher, F., 2005. High resolution room-temperature sample scanning superconducting interference device microscope configurable for geological and biomagnetic applications. Rev. Sci. Instrum. 76, 053703.

Fuller, M., Cisowski, S.M., 1987. Lunar paleomagnetism. In: Jacobs, J.A. (Ed.), Geomagnetism 2. Academic Press, Orlando, pp. 307–455.

Fuller, M., Cisowski, S., Hart, M., Haston, R., Schmidke, E., Jarrard, R., 1988. NRM:IRM(s) demagnetization plots; an aid to the interpretation of natural remanent magnetization. Geophys. Res. Lett. 15, 518–521.

Fuller, M., Kidane, T., Ali, J., 2002. AF demagnetization characteristics of NRM, compared with anhysteretic and saturation isothermal remanence: an aid in the intrepretation of NRM. Phys. Chem. Earth 27, 1169–1177.

Furnes, H., 1980. Chemical changes during palagonitization of an akaline olivine basaltic hyaloclastite, Santa Maria, Azores. Neues. Jahrb. Mineral. Abh. 138, 14–30.

Gattacceca, J., Rochette, P., 2004. Toward a robust normalized magnetic paleointensity method applied to meteorites. Earth Planet. Sci. Lett. 227, 377–393.

Holt, J.W., Kirschvink, J.L., 1996. Geomagnetic field inclinations for the past 400 kyr from the 1-km core of the Hawaii Scientific Drilling Project. J. Geophys. Res. 101, 11655–11663.

Kent, D.V., Gee, J., 1996. Magnetic alteration of zero-age oceanic basalt. Geology 24, 703–706.

Kirschvink, J.L., 1980. The least-squares line and plane and the analysis of paleomagnetic data: examples from Siberia and Morocco. Geoph. J. Royal Astr. Soc. 62, 699–718.

Kletetschka, G., Kohout, T., Wasilewski, P.J., 2003. Magnetic remanence in the Murchison meteorite. Meteorit. Planet. Sci. 38, 399–405.

Kletetschka, G., Acuna, M.H., Kohout, T., Wasilewski, P.J., Connerney, J.E.P., 2004. An empirical scaling law for acquisition of thermoremanent magnetization. Earth Planet. Sci. Lett. 226, 521–528.

Kletetschka, G., Fuller, M.D., Kohout, T., Wasilewski, P.J., Herrero-Bervera, E., Ness, N.F., Acuna, M.H., 2006. TRM in low magnetic fields: a minimum field that can be recorded by large multidomain grains. Phys. Earth. Planet. Inter. 154, 290–298.

Koenigsberger, J., 1933. Zu der Bestimmung des magnetischen Erdfeldes in fruherer Zeit aus der Magnetisierung con gebrannten Tongegenstanden und von Gesteinen. Beitr. Geophysik 38, 47–52.

Kontny, A., Vahle, C., de Wall, H., 2003. Characteristic magnetic behavior of subaerial and submarine lava units from the Hawaiian Scientific Drilling Project (HDSP-2). Geochem. Geophys. Geosyst. 4, 8703. doi:10.1029/2002GC000304.

Laj, C., Kissel, C., 1999. Geomagnetic field intensity at Hawaii for the last 420 kyr from the Hawaii Scientific Drilling Project core, Big Island, Hawaii. J. Geophys. Res. 104, 15317–15338.

Morris, R.V., Golden, D.C., Ming, D.W., Shelfer, T.D., Jorgensen, L.C., Bell, J.F., Graff, T.G., Mertzman, S.A., 2001. Phyllosilicate-poor palagonitic dust from Mauna Kea Volcano (Hawaii): A mineralogical analogue for magnetic Martian dust? J. Geophys. Res. 106, 5057–5083.

Pick, T., Tauxe, L., 1994. Geomagnetic paleointensities during the Cretaceous normal superchron measured using submarine basalt glass. Nature 366, 129–139.

Schiffman, P., Watters, R.J., Thompson, N.W., A.W., 2006. Hyaloclastites and the slope stability of Hawaiian volcanoes: insights from the Hawaiian Scientific Drilling Project's 3-km drill core. J. Volcanol. Geotherm. Res. 151, 217–228.

Sharp, W.D., Renne, P.R., 2005. The $^{40}Ar/^{39}Ar$ dating of core recovered by the Hawaii Scientific Drilling Project (phase 2), Hilo, Hawaii. Geochem. Geophys. Geosyst. 6. doi:10.1029/2004GC000846 Q04G17.

Steveling, E., 2006. personal communication.

Steveling, E., Stoll, J.B., Leven, M., 2003. Quasi-continuous depth profiles of rock magnetization from magnetic logs in the HSDP-2 borehole, Island of Hawaii. Geochem. Geophys. Geosyst. 4, 8708.

Stroncik, N.A., Schminke, H.-U., 2002. Palagonite — a review. Int. J. Earth Sci. 91, 680–697.

Tauxe, L., Love, J.J., 2003. Paleointensity in Hawaiian Scientific Drilling Project Hole (HSDP2): results from submarine basaltic glass. Geochem. Geophys. Geosyst. 4, 8702. doi:10.1029/2001GC000276.

Thellier, E., 1937. Aimantation des terres cuites; application à la recherche de l'intensité du champ magnétique terrestre dans le passé. C. R. Acad. Sci. Paris 204, 184–186.

Verrier, V., Rochette, P., 2002. Estimating peak currents at ground lightning impacts using remanent magnetization. Geophys. Res. Lett. 29 (art. no.- 1867).

Walton, A.W., Schiffman, P., 2003. Alteration of hyaloclastites in the HSDP 2 Phase 1 Drill Core- 1. Description and paragenesis. Geochem. Geophys. Geosyst. 4, 8709. doi:10.1029/2002GC000368.

Weiss, B.P., Lima, E.A., Fong, L.E., Baudenbacher, F.J., 2007. Paleomagnetic analysis using SQUID Microscopy. J. Geophys. Res. 112, B09105. doi:10.1029/2007JB004940.

Yu, Y.J., 2006. How accurately can NRM/SIRM determine the ancient planetary magnetic field intensity? Earth Planet. Sci. Lett. 250, 27–37.